ACS Sustainable Chemistry & Engineering

pubs.acs.org/journal/ascecg

Research Article

Scalable Ambient Synthesis of Metal−Organic Frameworks and Their Derivative Nanoporous Carbon for Superior Potassium Ion Storage

Giwook Lee,[‡] Kangseok Kim,[‡] Eunho Lim, and Jongkook Hwang*

Cite This: ACS Sustainable Chem. Eng. 2024, 12, 14524−14533

Read Online

ACCESS | Metrics & More | Article Recommendations | Supporting Information

ABSTRACT: Large-scale production of metal−organic frameworks (MOFs) under standard atmospheric conditions is of significant interest due to their cost-effectiveness and energy efficiency. However, such approaches often require excessive organic ligands or harmful additives to overcome the substantial energy barrier for nucleation. In this study, we present a scalable synthesis of zinc MOFs ($[Zn_2(BDC)_2DABCO]_n$ (ZnBD)) with a high space-time yield exceeding 2400 kg m^{-3} day^{-1} under ambient conditions, employing only stoichiometric amounts of reactants and no additional additives. Zinc acetate forms soluble dimers that mimic the structure of the secondary building units (SBUs) of ZnBD. This structural similarity facilitates ligand exchange between acetate and organic ligands, thereby lowering the energy barrier for nucleation. The *in situ*-generated acetate anions further enhance ZnBD production by promoting the deprotonation of the organic ligands. Additionally, these acetate anions serve as coordination modulators, enabling the production of one-dimensional nanorod crystals with controlled sizes and aspect ratios. As a proof of concept, ZnBD is transformed into N/O-co-doped nanoporous carbon through pyrolysis in an Ar atmosphere, demonstrating its potential as an anode material for potassium-ion batteries. The results of this study advance the facile large-scale production of ZnBD and expand the application potential of ZnBD-derived materials.

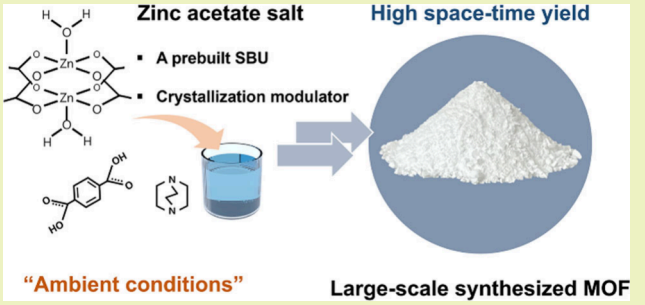

KEYWORDS: *Pillar-layered MOF, Metal acetate, Scalable synthesis, Ambient condition, MOF-derived carbons, Potassium ion batteries*

INTRODUCTION

Metal−organic frameworks (MOFs) are crystalline porous materials formed by linking metal-containing nodes, known as secondary building units (SBUs), with multitopic organic ligands.[1] Among the most extensively studied MOFs are pillar-layer MOFs, which use two types of ligands (a layer-bridging ligand and a pillar ligand) simultaneously to achieve high structural and chemical tunability.[2] The flexibility of combining mixed ligands allows the creation of various pillar-layer MOFs with precisely tailored pore structures and topologies at the molecular level.[3] $[M_2(BDC)_2DABCO]_n$ (M = metal, BDC = 1,4-benzenedicarboxylic acid, DABCO = 1,4-diazabicyclo-[2,2,2]octane) (MBD) is a prototypical pillar-layer MOF in which the DABCO pillar connects two-dimensional (2D) M-BDC layers to form three-dimensional (3D) structures (Figure S1).[4,5] Given their structural flexibility and responsiveness to different guests and external physical stimuli, MBDs are employed in various applications, such as gas adsorption, polymerization, and solid-state structural transformation.[6−12] Additionally, similar to other MOFs, MBDs have recently gained significant attention as versatile self-templates for synthesizing various carbon-based composite materials with controllable pore structures and surface areas.[13−15] The BDC and DABCO ligands provide carbon and heteroatom sources, enabling the direct synthesis of porous carbon materials doped with oxygen and nitrogen through simple pyrolysis. These MBD-derived carbons are used in several applications, including hybrid supercapacitor and catalysts.[10,16]

However, the widespread use of MBDs and their derivatives has been limited because of challenges in large-scale production.[17−19] In laboratory settings, MBDs are commonly synthesized via solvothermal reactions in a sealed vessel at elevated temperatures exceeding 120 °C and under autogenic pressure. Scaling up this method is challenging because the reaction duration can be long, and the MBD quality highly depends on the vessel's size.[20] Consequently, the rapid synthesis of MBDs under ambient conditions is attracting significant attention as a cost-effective and environmentally friendly alternative that reduces energy consumption.[21] Despite several reports on ambient synthesis of MBDs and

Received: July 21, 2024
Revised: August 31, 2024
Accepted: September 11, 2024
Published: September 19, 2024

other MOFs, these methods often involve the use of excess organic ligands or base additives to promote rapid nucleation at ambient temperatures.[21−23] However, organic bases are toxic, corrosive, and expensive, thereby increasing the overall cost of MOF production.[20] MBDs are generally produced in milligram quantities without base additives, with low production yields of less than 15% under ambient conditions.[23]

One promising strategy to overcome this challenge is the prebuilt SBU approach, which ensures the high quality and productivity of the desired MOFs without the need for additives.[24,25] By exploiting the structural similarity between the designed inorganic clusters and the SBUs of MOFs, this method reduces the activation barriers for MOF nucleation, allowing rapid reaction kinetics under milder conditions.[25−27] However, the design and synthesis of prebuilt SBUs have become a bottleneck, hindering the widespread adoption of this strategy. Recently, our research group has demonstrated that acetate salts can serve as natural prebuilt SBUs in the room-temperature synthesis of MBDs, eliminating the need for synthesizing controlled inorganic clusters.[28] In a dimethylformamide (DMF) solution, the acetate salt maintains a coordination structure similar to that of the paddle wheel SBU of MBD, enabling rapid nucleation and high-yield MBD crystal production.[29,30] However, these findings were validated only under highly dilute conditions, and the impact of *in situ*-generated acetate anions during nucleation was not considered. Therefore, it remains an open question whether large-scale production of MBD with high yields is possible without compromising the purity and quality of MBD when using high acetate salt concentrations.

In this study, we demonstrate the synthesis of ZnBD on a tens-of-gram scale in a 1-L beaker under ambient conditions without excessive ligands or toxic additives. Our findings indicate that zinc acetates are crucial for the production of high-quality, phase-pure ZnBDs with a Kagome structure within a few minutes. The structural similarity between acetate-bridged dimers and the SBUs of the ZnBD (paddle-wheel structure), combined with the basicity of *in situ*-generated acetate anions, accelerates nucleation, leading to the rapid formation of ZnBDs with a production yield exceeding 90% and a space-time yield (STY) exceeding 2400 kg m^{-3} day^{-1}. To broaden the application scope of ZnBD, it was transformed into an N/O-co-doped nanoporous carbon material via simple pyrolysis in an Ar gas atmosphere and tested as an anode material for potassium-ion batteries (PIBs). The ZnBD-derived carbon (ZDC) exhibited a high capacity of 370 mAh g^{-1} at 30 mA g^{-1} and excellent capacity retention of 95.6% after 300 cycles of potassiation/depotassiation at 1000 mA g^{-1}. These results suggest that ZDCs have significant potential for various applications, including as anode materials for PIBs.

EXPERIMENTAL SECTION

Chemicals. The following chemicals were used as received from commercial sources: acetic acid (CH_3COOH, glacial, 99.5%, Samchun), aluminum chloride hexahydrate ($AlCl_3·6H_2O$, 99%, Sigma-Aldrich), 1,4-diazabicycle[2,2,2]octane (DABCO, ≥98%, Millipore), N,N-dimethylformamide (DMF, 99.9%, Samchun), furfuryl alcohol (FA, 98%, Sigma-Aldrich), hydrochloric acid (HCl, 35.0−37.0%, Samchun), hydrofluoric acid (HF, 48%, Sigma-Aldrich), tetraethyl orthosilicate (TEOS, 98%, Sigma-Aldrich), pluronic P123 ($EO_{20}PO_{70}EO_{20}$, Sigma-Aldrich), terephthalic acid (H_2BDC, ≥98%, Millipore), zinc acetate dihydrate ($Zn(OAc)_2·2H_2O$, ≥98%, Sigma-Aldrich), zinc nitrate hexahydrate ($Zn(NO_3)_2·6H_2O$, ≥98%, Sigma-Aldrich).

Materials Preparation. All reactants were dissolved in DMF solution at a stoichiometric molar ratio (Zn^{2+}:H_2BDC:DABCO = 2:2:1). The synthesized ZnBD was denoted as ZnBD-*c* (where *c* represents the concentration of zinc acetate in [mM]). In ZnBD-10 synthesis, solutions of zinc acetate (0.263 g, 1.2 mmol in 10 mL DMF), DABCO (0.067 g, 0.6 mmol in 10 mL DMF), and H_2BDC (0.199 g, 1.2 mmol in 100 mL DMF) were prepared separately. The zinc acetate and DABCO solutions were sequentially added dropwise (2 mL min^{-1}) to the BDC solution while stirring at 300 rpm for 10 min. The precipitated ZnBD was collected by centrifugation, thoroughly washed with DMF, and dried at 150 °C for 20 h under vacuum to determine the final yield. ZnBD-60 was prepared following the ZnBD-10 synthesis, while solutions of zinc acetate (1.580 g, 7.2 mmol in 10 mL DMF), DABCO (0.404 g, 3.6 mmol in 10 mL DMF), and H_2BDC (1.196 g, 7.2 mmol in 100 mL DMF) were used. For synthesis of ZnBD-120, solutions of zinc acetate (3.161 g, 14.4 mmol in 10 mL DMF), DABCO (0.807 g, 7.2 mmol in 10 mL DMF), and H_2BDC (2.392 g, 14.4 mmol in 100 mL DMF) were used. For a control experiment involving the addition of acetic acid to the ZnBD-10 synthesis conditions, acetic acid (0.687 mL) was added to the zinc acetate/BDC mixture. The concentrations of the reactants were identical to those used in the ZnBD-10 synthesis. In our synthesis condition, the saturated concentration for zinc acetate is 120 mM. For ZnBD-bulk synthesis, the ZnBD-120 conditions were scaled up by a factor of 7.

To prepare ZnBD-derived carbon (ZDC), the ZnBD-bulk was carbonized at 600 °C for 2 h under Ar gas flow in a horizontal tubular furnace with a ramp rate of 2 °C min^{-1}. The carbonized samples were then washed with 1 M HCl overnight at room temperature, rinsed with distilled water, and dried at 100 °C overnight.

CMK-3 was synthesized following a previously described method using SBA-15 as a hard template.[31] For the synthesis of SBA-15, P123 (24 g) was dissolved in 750 mL of 1.6 M HCl solution at 40 °C. TEOS (54.6 mL) was then added to the solution and stirred for 24 h. The resulting mixture was subjected to hydrothermal treatment at 100 °C for 24 h. The precipitate was filtered, washed, and dried at 80 °C. To remove the soft template, the product was calcined at 550 °C for 4 h under static air at a ramp rate of 5 °C min^{-1}. To synthesize CMK-3, aluminated SBA-15 was filled with FA and thermally treated at 80 °C for 3 h to polymerize FA. The resulting powder was carbonized at 900 °C for 4 h under Ar flow in a horizontal tubular furnace, with a ramp rate of 1 °C min^{-1} until 600 and 5 °C min^{-1} until 900 °C. The carbonized samples were washed with 10 wt % HF overnight, rinsed with distilled water, and dried at 100 °C.

Characterization. The morphologies of the ZnBDs and carbons were examined using scanning electron microscopy (SEM) (Hitachi S-4800, 15.0 kV) and transmission electron microscopy (TEM) (JEOL JEM-2100F, 200 kV). The crystal structures were evaluated by powder X-ray diffraction (XRD) using Cu Kα radiation (λ = 0.154 nm, Rigaku D/max-2500 V/PC). Thermogravimetric analysis (TGA) was performed using a simultaneous thermal analyzer-mass spectrometer (NETZSCH STA449 F3) under a continuous nitrogen gas flow in alumina pans at a heating rate of 10 °C min^{-1} up to 1000 °C. Gas physisorption measurements were conducted with nitrogen at 77 K and CO_2 at 273 K using a Quantachrome Autosorb iQ instrument. Before analysis, the samples were degassed at 150 °C for 20 h. The isotherms were analyzed using the QuadraWin software (version 5.1). Surface areas were determined using the Brunauer−Emmett−Teller (BET) method with a multipoint BET model (P/P_0 = 0.003−0.05). Pore size distributions of the MOFs were computed using a cylindrical pore nonlocal density functional theory (NLDFT) equilibrium model for N_2 adsorbed on silica. The pore size distributions of ZDC and CMK-3 were computed using a cylindrical pore quenched solid DFT (QSDFT) adsorption branch for N_2 adsorbed on carbon and an NLDFT model for CO_2 adsorbed on carbon. Proton nuclear magnetic resonance (^{1}H NMR) spectroscopy was performed using a Jeol Resonance ECZ600R (600 MHz) spectrometer. Raman spectroscopy was conducted using a Raman

https://doi.org/10.1021/acssuschemeng.4c06002
ACS Sustainable Chem. Eng. 2024, 12, 14524−14533

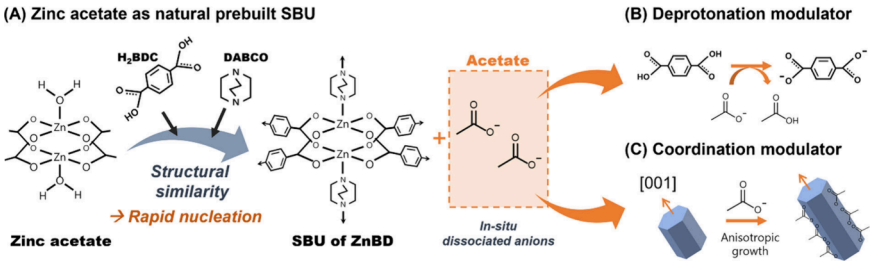

Figure 1. Triple function of zinc acetate salt in the scalable synthesis of ZnBD under ambient condition: (A) natural prebuilt SBU, (B) deprotonation modulator, and (C) coordination modulator.

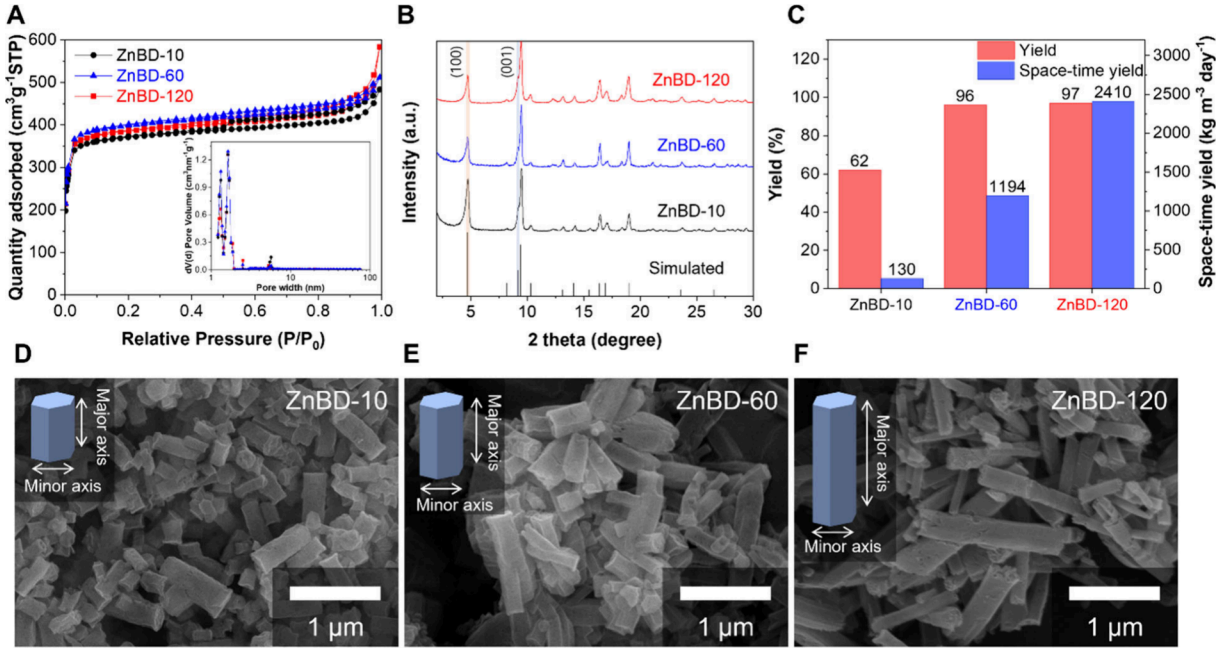

Figure 2. Characterization of ZnBD-*c* prepared using different concentrations of zinc acetate (*c* = 10, 60, and 120 mM) at the same reaction time (10 min). (A) N_2 physisorption isotherms (inset: differential pore size distributions), (B) XRD patterns, and (C) yield and space-time yield of the ZnBDs. SEM images of (D) ZnBD-10, (E) ZnBD-60, and (F) ZnBD-120.

spectrometer (Horiba Jobin Yvon, LabRam HR Evolution) with a 532 nm laser. X-ray photoelectron spectroscopy (XPS) analysis was conducted using a ThermoFisher Scientific NEXSA X-ray photoelectron spectrometer. Elemental analysis was performed using an elemental analyzer (TRSMCHNSC - 6280TRSM, LECO).

The yield of ZnBDs was calculated by following equation

$$\text{yield} = \frac{\text{actual yield}}{\text{theoretical yield}} \times 100(\%)$$

The space-time yield (STY) of ZnBDs was calculated by following equation

$$\text{STY} = \frac{\text{mass of MOF production (kg)}}{\text{volume of reaction mixture (m}^3\text{)} \times \text{reaction time (day)}}$$

Electrochemical Measurements. The electrochemical performance of the porous carbon materials was evaluated in a CR2032-type coin-cell configuration using K metal as both the counter and reference electrodes. The coin cells were assembled in an Ar-filled glovebox. A slurry was prepared by mixing porous carbon material, carbon black (Super P, Alfa Aesar), sodium carboxymethyl cellulose (CMC, Sigma-Aldrich), and styrene−butadiene rubber (SBR, MTI Korea) in a weight ratio of 70:10:10:10, yielding a paste using deionized water. The slurry was applied to a copper foil current collector (MTI, Korea) using a doctor blade. The electrode was dried at 80 °C for 15 h under vacuum and then pressed with a roll press. The mass loading of the active material in the electrode was 0.6−0.8 mg cm^{-2}. Additionally, a solution of 1.0 M KFSI dissolved in ethylene carbonate and diethyl carbonate (EC:DEC = 1:1 vol %) was used as the electrolyte. A GF/F glass microfiber filter (Whatman, USA) was used as the separator. Galvanostatic charge/discharge (GCD) tests and cyclic voltammetry (CV) were performed at 30 °C using a WBCS-3000 battery cycler (WonATech Co.). The GCD tests of the electrodes were conducted within a potential range of 0.01−3.0 V (vs K^+/K). CV analysis of the anode was performed in the potential range 0.01−3.0 V at scan rates ranging from 0.1 to 10 mV s^{-1}. Electrochemical impedance spectroscopy (EIS) was performed using an electrochemical workstation ZIVE BP2 (WonATech Co.) in the frequency range 100 kHz to 10 mHz with an AC oscillation of 10 mV.

RESULTS AND DISCUSSION

Scalable ZnBD Synthesis under Ambient Conditions. We expect that zinc acetate salts will play three critical roles in the synthesis of ZnBD under ambient conditions (Figure 1). First, zinc acetate functions as a prebuilt SBU, forming soluble paddle-wheel $Zn_2(OAc)_4{\cdot}(H_2O)_2$ dimers similar in structure to the $(Zn_2(BDC)_4{\cdot}(DABCO)_2)$ SBU of ZnBD (Figure 1A).[28,29] This facilitates rapid ligand exchange between acetate and BDC, allowing the formation of Zn-BDC layers through homogeneous nucleation within seconds. Second, as Zn-BDC

https://doi.org/10.1021/acssuschemeng.4c06002
ACS Sustainable Chem. Eng. 2024, 12, 14524−14533

layer form, acetate anions dissociate, increasing the concentration of free acetate in the reaction medium.[20] The basicity of the generated acetate anions enhances the deprotonation of the H_2BDC ligand, thereby further facilitating nucleation and improving the production yield (Figure 1B).[32,33] Third, acetate anions serve as coordination modulators that inhibit the growth of Zn-BDC layers while promoting the development of Zn-DABCO layers along the [001] direction (Figure 1C).[34] This modulation influences the size and morphology of ZnBD, leading to larger particle sizes and one-dimensional (1D) anisotropic morphologies at higher free acetate concentrations.

We dissolved various concentrations of zinc acetate in DMF-d_7 and conducted a ^{1}H NMR analysis to confirm that the zinc acetate solutions contained acetate-bridged $Zn_2(OAc)_4 \cdot (H_2O)_2$ dimers (i.e., natural prebuilt SBU). If zinc acetate retained its dimeric acetate-bridged $Zn_2(OAc)_4 \bullet (H_2O)_2$ structures, no ^{1}H NMR signals from dissociated acetate anions would be observed. Across all concentrations, the ^{1}H NMR spectra show only the proton signal of $-CH_3$ and no signal attributed to $-COOH$ (Figure S2). These findings indicate that no free acetate is detectable in DMF solutions and that zinc acetate does not dissociate into Zn^{2+} cations and acetate anions, even in saturated zinc acetate solutions. Instead, it maintains dimeric acetate-bridged structures, suggesting that zinc acetate can act as a prebuilt SBU regardless of its concentration, facilitating the rapid formation of Zn-BDC layers and ZnBD nuclei. These results in good agreement with previous literature.[28,29]

We then adjusted the acetate salt concentration to investigate the effect of *in situ*-generated acetate on the nucleation and growth of ZnBD. The resulting ZnBD is denoted as ZnBD-*c*, where *c* represents the zinc-ion concentration in [mM]. ZnBD-*c* was prepared at different concentrations (10, 60, and 120 mM) and maintained the same reaction time (10 min). N_2 physisorption isotherms for the ZnBDs indicated gas saturation at a low relative pressure below $P/P_0 \sim 0.05$, corresponding to the type-I behavior of microporous materials (Figure 2A). Pore size distributions (PSD) of ZnBDs were estimated using a cylindrical pore NLDFT equilibrium model, which displayed comparable PSDs with micropores ranging from 1.3 to 1.6 nm. These materials also exhibit high specific surface area ($\sim$1500 $m^2\ g^{-1}$) and microporosities similar to those of previously reported ZnBDs (Table S2). All ZnBDs exhibited XRD patterns that matched well with the hexagonal Kagome structures without any impurity phases (Figure 2B).

Noteworthy is the significant variation in yield and STY among the samples (Figure 2C). ZnBD-120 exhibited exceptionally high yield (97%) and STY (2410 kg m^{-3} day^{-1}), which were much higher than those of ZnBD-60 and ZnBD-10. This high STY is comparable to previously reported industrial MOF production processes (Table S3). Notably, STY is a better metric for assessing large-scale production feasibility because it quantifies the amount of MOFs produced per unit volume of the reaction mixture and per unit time.[20] The reaction rate and productivity improved as the zinc acetate concentration increased. These observations can be attributed to the rise in the acetate anion concentration, which occurs alongside the formation of the Zn-BDC layer. Acetate ions, which are weakly basic, facilitate the deprotonation of H_2BDC, thereby enhancing their nucleation rate and production yield.[32,33] Consequently, the yield increased substantially from 62% for ZnBD-10 to 96% for ZnBD-60. ZnBD-120 achieved a yield similar to that of ZnBD-60 but at twice the concentration, leading to a doubling of the STY.

The SEM images reveal that all ZnBD samples exhibit an anisotropic 1D nanorod morphology (Figure 2D–F). However, as the zinc acetate concentration was increased from 10 to 60 to 120 mM, the average length of the major axis increased from 450 to 590 to 1270 nm, respectively, while the minor axis remained approximately 200 nm. This change significantly increased the aspect ratio of the major axis from 2.15 to 2.87 to 5.0 (Figure S3). The morphological changes of ZnBD-*c* were further confirmed by the corresponding changes in the XRD patterns (Figure 2B). We compared the peak intensities of the (100) and (001) surfaces of ZnBD-*c* in these XRD patterns. As the concentration of the reactants increased from ZnBD-10 to ZnBD-60 to ZnBD-120, the intensity ratio of the (100) to (001) peak notably increased, from 0.50 to 0.68 to 0.95, respectively. The increase in the intensity ratio is consistent with the trend of increasing aspect ratios of ZnBD particles. This XRD result further supports the preferential growth of the (001) plane, which corresponds to the Zn-DABCO-terminated surface.[35] This anisotropic crystal growth can be attributed to the coordination-modulating properties of acetate, a monocarboxylate ligand.[34] As shown in Figure S1, the growth of ZnBD is governed by two coordination modes: Zn-BDC and Zn-DABCO. ZnBDs feature two hexagonal (001) end faces terminated by Zn-DABCO bonds, with the remaining six faces terminated by Zn-BDC bonds. Acetate, a well-known monodentate ligand, competes with BDC ligands for zinc coordination. Because BDC and acetate possess identical carboxylate functionalities, the presence of acetate impedes the interaction between zinc and BDC. This competitive interaction reduced the reactivity of Zn-BDC layers, thereby inhibiting their growth (Figure 1C). Consequently, the relatively high-energy Zn-DABCO (001) surfaces are minimized through preferential anisotropic growth along the [001] direction.[9] Similarly, additional experiments involving the addition of acetic acid to the ZnBD-10 synthesis conditions confirmed an increase in the length of the major axis, resulting in a higher aspect ratio of the crystals (Figure S4). Therefore, it can be concluded that the *in situ*-generated acetate acts as a coordination modulator and that a higher concentration of acetate promotes the formation of high-aspect-ratio nano/microrods by selectively inhibiting their growth on the Zn-BDC surfaces.

We further examined the effect of reaction time on the growth of the MOF at the same concentration of 120 mM. By varying the reaction time to 10, 30, and 60 min, we observed no significant differences in the overall properties (e.g., specific surface area, particle size, crystal phase) and production yield of ZnBD (Figure S5). This suggests that a 120 mM concentration and a 10 min reaction time are optimal synthesis conditions considering STY and MOF quality because the growth of ZnBDs is mostly completed within the first 10 min.

Under optimized experimental conditions, we scaled up the standard ZnBD-120 synthesis by a factor of 7 to produce bulk ZnBD (denoted as ZnBD-bulk). We synthesized 28.6 g in a single 1-L beaker, achieving a yield of 98% and an STY of 2454 kg m^{-3} day^{-1}, while maintaining crystal quality comparable to that of the reference (Figure 3). This result demonstrates our ability to mass-produce ZnBD with high STY without compromising the purity or quality, highlighting its significant potential for large-scale synthesis.

https://doi.org/10.1021/acssuschemeng.4c06002
ACS Sustainable Chem. Eng. 2024, 12, 14524−14533

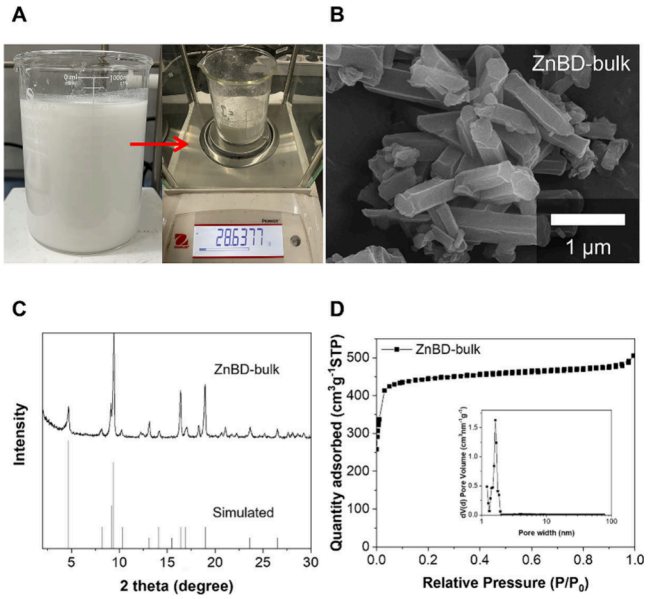

Figure 3. (A) Photograph showing the quantity of ZnBD-bulk synthesized at a 1 L beaker scale. (B) SEM image, (C) XRD pattern, and (D) N_2 physisorption isotherm (inset: corresponding differential PSDs) of ZnBD-bulk.

Notably, zinc acetate is crucial for the large-scale synthesis of ZnBD under ambient conditions. In a control experiment in which zinc acetate was replaced with zinc nitrate under identical synthesis conditions, a significantly lower yield (approximately 15%) and STY (120 kg m^{-3} day^{-1}) were achieved (Figure S6). The significant lack of soluble paddle wheel dimers in the zinc nitrate solution slowed nucleation, resulting in a considerably lower yield of ZnBD.[30] Furthermore, the oxidative nature of nitrates presents a considerable risk of explosive reactions during MOF production. The use of chlorides, meanwhile, gives rise to the necessity for additional preventive measures against corrosion, thereby increasing operational costs. In comparison, zinc acetates are generally safer and pose fewer safety risks, especially when scaling up production methods.[20]

Thermal Transformation of ZnBD to ZDC. The ZnBD-bulk was transformed into ZnBD-derived carbon (ZDC) by pyrolysis under an argon atmosphere at 600 °C, followed by washing with 1 M HCl. Electron microscopy images (Figure 4A) indicate that ZDC retained the rod-like morphology of the parent ZnBD. The images also reveal a highly porous structure with randomly and homogeneously distributed mesopores (Figure 4A). XRD analysis confirms the amorphous nature of ZDC and the absence of crystalline Zn residues (Figure 4B).[36] The Raman spectrum of ZDC shows two distinct bands corresponding to the D-band (1342 cm^{-1}) and G-band (1596 cm^{-1}) (Figure 4C). The I_D/I_G intensity ratio was approximately 0.80, indicating typical amorphous carbon properties (Table S4).[37] Furthermore, the nitrogen content of ZDC was approximately 1.9 at%, originating from the DABCO ligand, as verified by the XPS analysis (Table S4). The N 1s XPS spectrum was deconvoluted into graphitic N (401.3 eV), pyrrolic N (400.2 eV), and pyridinic N (398.3 eV) (Figure 4D).[38] The deconvoluted O 1s XPS spectrum highlights the presence of oxygen functional groups, with O−C = O carboxylic (533.8 eV), C−O ether (532.5 eV), and C = O carbonyl (531.7 eV) groups in ZDC (Figure 4E).[39] XPS analysis confirmed that nitrogen and oxygen species were successfully codoped into the ZDC, potentially enhancing the electrochemical performance of PIB anodes.[40] N_2 physisorption at 77 K was conducted to characterize the pore structures and surface area of ZDC (1138 m^2 g^{-1}). ZDC exhibits a type

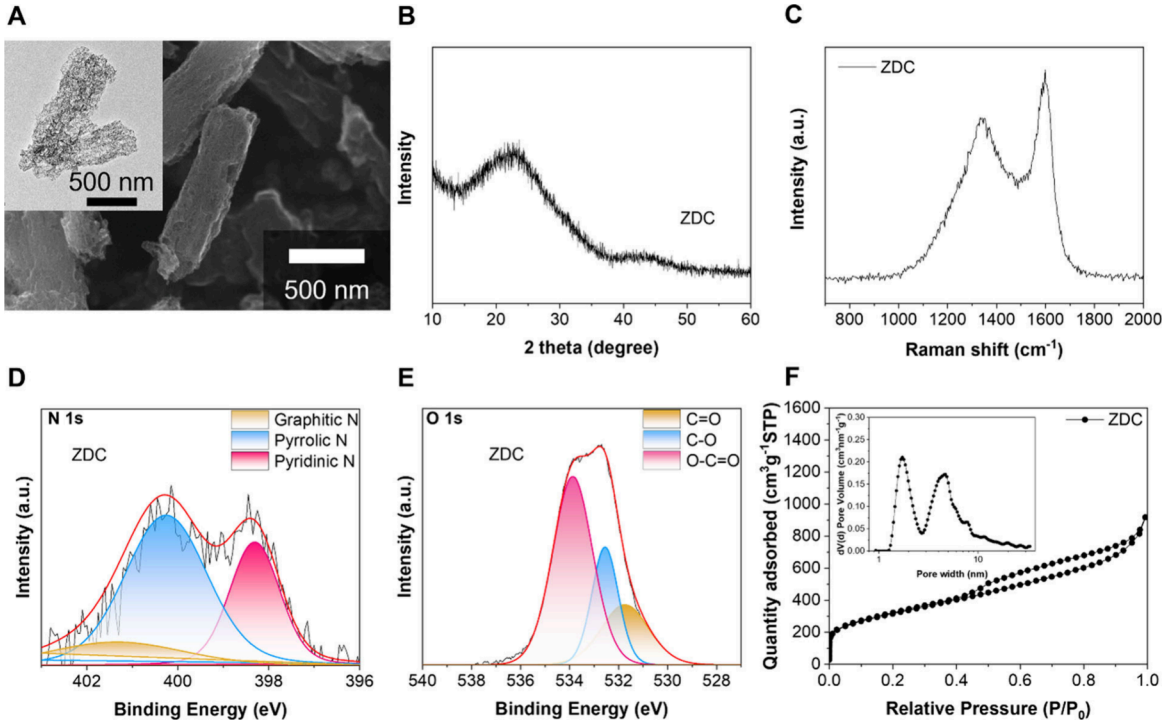

Figure 4. Characterization of ZDC. (A) SEM image (inset: corresponding TEM image). (B) XRD pattern. (C) Raman spectra. High-resolution XPS spectra of (D) N 1s and (E) O 1s. (F) N_2 physisorption isotherms at 77K (inset: corresponding differential PSDs).

https://doi.org/10.1021/acssuschemeng.4c06002
ACS Sustainable Chem. Eng. 2024, 12, 14524−14533

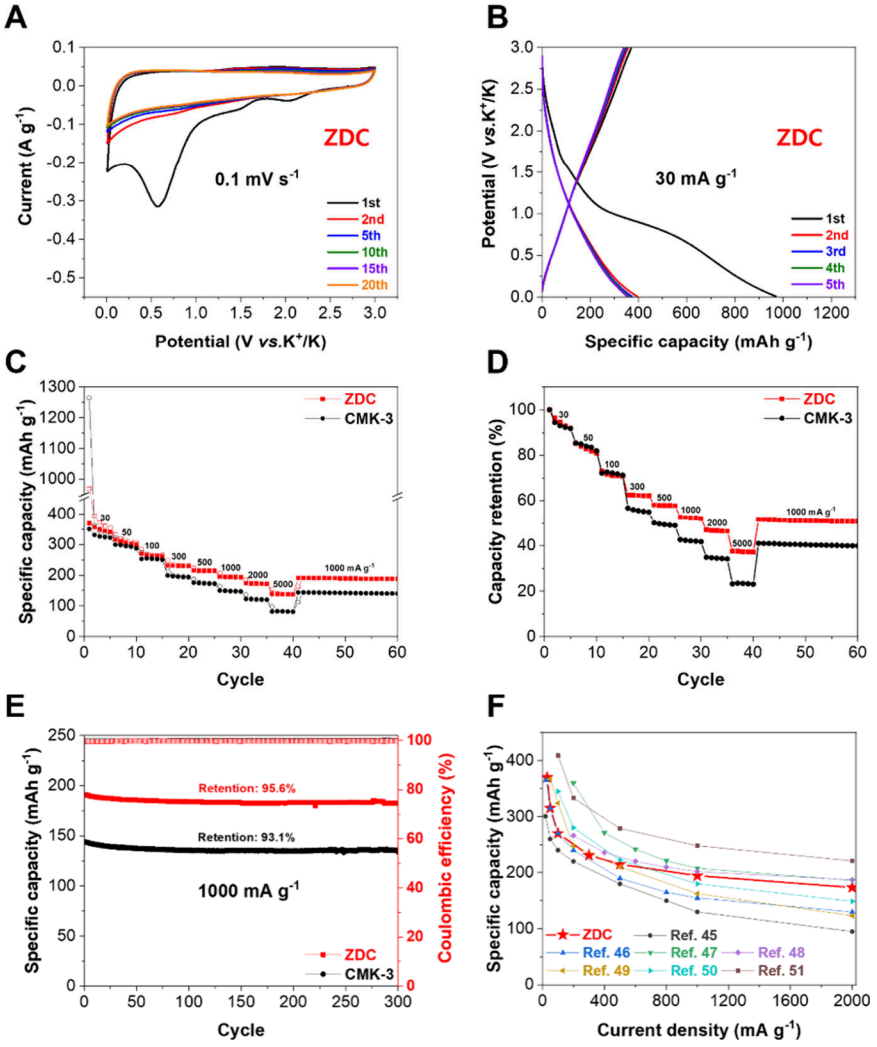

Figure 5. (A) CV profiles of ZDC for the 1st to 20th cycles at 0.1 mV s^{-1}. (B) GCD profiles of ZDC for the first five cycles at 30 mA g^{-1}. (C) Rate performance and (D) capacity retention of porous carbon anodes at different current densities 30 to 5000 mA g^{-1}. (E) Cycling performance of porous carbon anodes at 1000 mA g^{-1}. (F) Comparison of K^+ storage performance of ZDC and previously reported MOF-derived carbon anodes.

IV isotherm with significant N_2 uptake at low P/P_0 < 0.05 and a hysteresis loop at intermediate P/P_0 (0.45−0.95), indicative of the presence of micropores and mesopores (Figure 4F). PSDs confirmed that ZDC has a hierarchical pore system consisting of micropores (∼1.7 nm) and mesopores (∼4 nm) (Figure 4F), which are formed by the thermal decomposition of organic ligands and the removal of Zn species.[41] This hierarchical pore structure is advantageous for energy storage applications because it offers a high surface area due to micropores and enhanced mass transport through mesopores.[38] Given that the textural properties and concentrations of C, O, and N atoms can be tailored for specific applications by simply varying pyrolysis conditions—such as temperature, ramping rate, retention time, and gas atmosphere—or by altering the Zn removal method (either through HCl etching or vaporization at temperatures above 900 °C), the resulting ZDC materials hold great potential for a variety of applications, including electrode materials for sodium or potassium ion batteries, supercapacitors, capacitive deionization, and adsorbents for various molecules.[14,41−46]

Electrochemical Performance of ZDCs in Potassium-Ion Storage. Owing to their abundant and inexpensive potassium resources, PIBs have garnered significant attention as a potential next-generation energy storage solution. Moreover, the standard redox potential of potassium (K^+/K) is comparable to or even lower than that of lithium (Li^+/Li) in nonaqueous electrolytes.[42] Despite these advantages, the development of high-performance anode materials remains a challenge. Recently, amorphous hard carbon materials have shown promise owing to their abundant defects, short-range order, and large interlayer spacing, which collectively enhance their rate performance and cyclic stability.[43] Among these amorphous carbons, MOF-derived carbon has been identified as particularly suitable for PIB anodes. MOF-derived carbon retains the high surface area and microporosity of the original MOFs and incorporates heteroatoms from organic ligands as dopants, thereby improving the storage kinetics and K^+ storage capacity.[44] Our research demonstrated that ZDC is a highly promising candidate for PIB anode materials. CMK-3, a benchmark-ordered mesoporous carbon characterized by arrays of hexagonal nanorods, was synthesized as a reference material to compare its electrochemical performance with that of ZDC (Figure S7). The physicochemical properties of ZDC and CMK-3 are summarized in Table S4. Although CMK-3 exhibited a higher surface area, pore volume, and degree of

https://doi.org/10.1021/acssuschemeng.4c06002
ACS Sustainable Chem. Eng. 2024, 12, 14524−14533

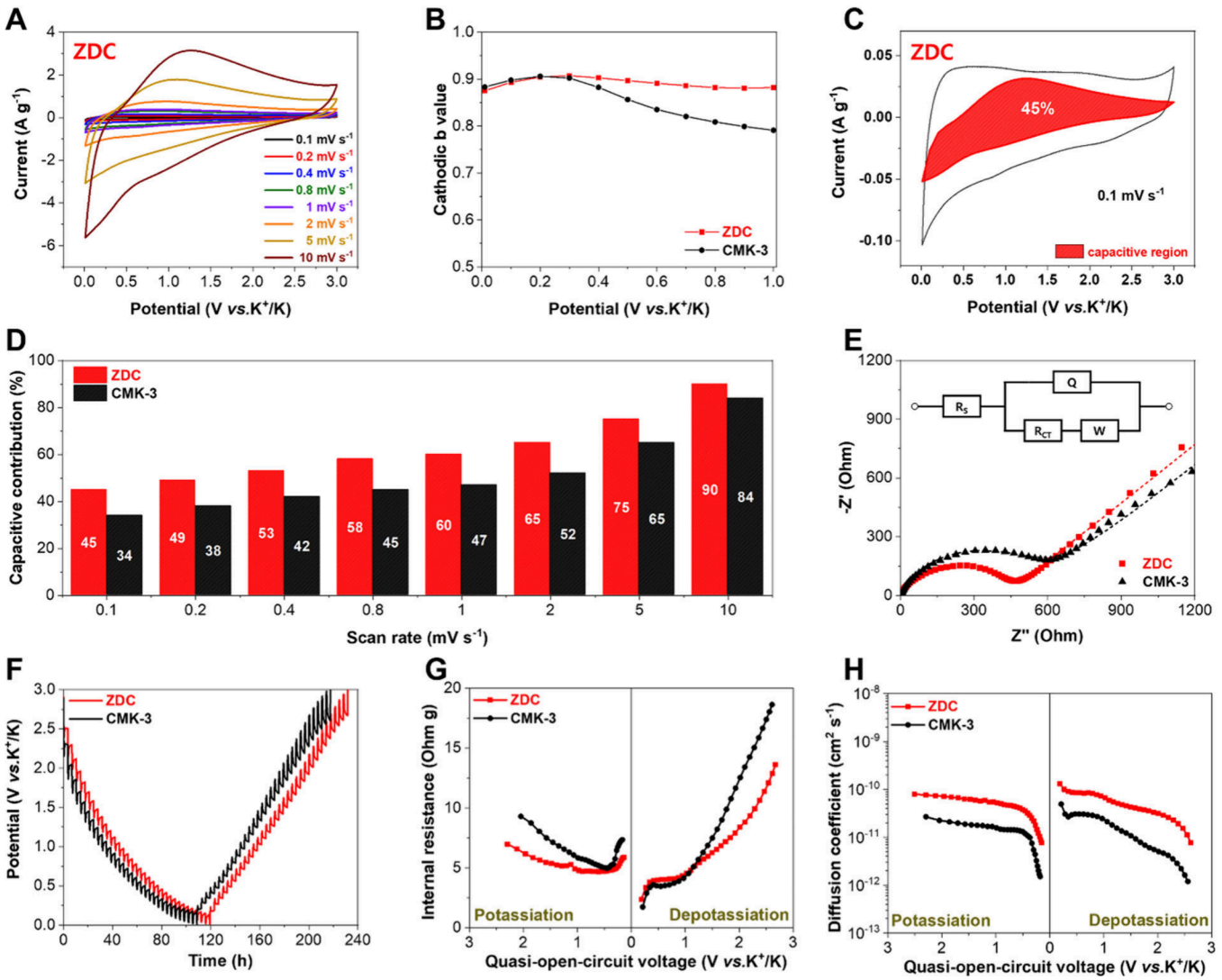

Figure 6. (A) CV profiles of ZDC at various scan rates in the range of 0.1−10 mV s^{-1}. (B) *b* values obtained by linearly fitting the logarithm of scan rate and peak current. (C) Capacitive contribution of ZDC obtained at a scan rate of 0.1 mV s^{-1}. (D) Comparison of the capacitive contributions of porous carbon anodes at different scan rates ranging from 0.1 to 10 mV s^{-1}. (E) Nyquist profiles of porous carbon anodes after 5 cycles at 50 mA g^{-1} (inset: equivalent circuit model for fitting Nyquist profiles). (F) GITT tests of the porous carbon anodes. (G) Electrode internal resistance and (H) solid-state diffusion coefficient of K^+.

graphitization than ZDC, it had a lower content of heteroatoms (O and N) than ZDC.

In half-cell tests, porous carbon samples were used as anode materials to evaluate their electrochemical K^+ storage performance. GCD and CV experiments were conducted in the potential range of 0.01−3.0 V (vs. K^+/K) with K metal as both the counter and reference electrodes. Figure 5A and Figure S8 show the CV profiles of the porous carbon anodes from the first to the 20th cycle at a scan rate of 0.1 mV s^{-1}. The sharp cathodic peaks are observed in the first cycle but disappear in subsequent cycles. These irreversible peaks are attributed to the formation of a solid electrolyte interphase (SEI) layer during the initial potassiation step and irreversible side reactions such as K^+ trapping in defects or functional groups and electrolyte decomposition.[39] After the first cycle, nearly overlapping CV profiles were observed, indicating a stable and reversible electrochemical reaction. Consistent with the CV results, the GCD profiles for the first five cycles at 30 mA g^{-1} showed overlap after an initial irreversible capacity loss during the first potassiation step (Figure 5B, Figure S9). ZDC exhibited an initial Coulombic efficiency (ICE) of 38.2%, higher than that of CMK-3 (27.7%). This is because ZDC has a lower specific surface area than CMK-3, which reduces the contact area available for electrolyte reduction and other surface-related side reactions.

The rate performance of the porous carbon anodes was evaluated using GCD tests conducted at various current densities ranging from 30 to 5000 mA g^{-1} (Figure 5C). The ZDC anodes demonstrated specific capacities of 370, 315, 270, 231, 215, 195, 174, and 139 mAh g^{-1} at current densities of 30, 50, 100, 300, 500, 1000, 2000, and 5000 mA g^{-1}, respectively. These anodes exhibited stable and reversible cycles even at high current densities (Figure S10). Moreover, ZDC showed a higher specific capacity than CMK-3 at all tested current densities and superior rate capability, achieving a capacity of 139 mAh g^{-1} at a high current density of 5000 mA g^{-1}. The disparity in rate performance is more pronounced when capacity values are normalized to depotassiation capacities at 30 mA g^{-1} (Figure 5D). ZDC maintained a significantly higher capacity retention than CMK-3 across all current densities.

https://doi.org/10.1021/acssuschemeng.4c06002
ACS Sustainable Chem. Eng. 2024, 12, 14524−14533

Additionally, ZDC retained 95.6% of its capacity after 300 cycles at 1000 mA g^{-1}, whereas CMK-3 retained 93.1% capacity under the same conditions (Figure 5E). The K^+ storage performance of ZDC was comparable to previously reported MOF-derived carbons and the state-of-the-art carbonaceous materials, demonstrating the potential of ZDC as a promising PIB anode material (Figure 5F, Table S5).[45−51]

Revealing the Potassium-Ion Storage Kinetics in the ZDC. To further investigate the kinetics and K^+ storage mechanism of the porous carbon anodes, CV analysis was performed at scan rates ranging from 0.1 to 10 mV s^{-1} (Figure 6A, Figure S11). The relationship between the scan rate (v) (mV s^{-1}) and peak current (i) (A g^{-1}) adheres to Equation 1, where a and b are adjustable parameters.

$$i = av^b \tag{1}$$

The b values were determined as the slope of the log(v) versus log(i) plot at cathodic currents over various potentials from 0.01 to 1 V (vs. K^+/K) (Figure 6B). The b value is typically used to estimate the potassiation mechanism, with a value of 0.5 indicating a diffusion-controlled process and 1.0 indicating a capacitive-controlled process.[52] Comparing the b values at the cathodic current peak, ZDC exhibited a value closer to 1 than CMK-3 at nearly all voltage ranges. These findings suggest that a surface-driven charge storage mechanism (capacitive-controlled behavior) is significantly dominant in ZDC. Additionally, we quantitatively separated the capacitive- and diffusion-controlled contributions using eq 2:

$$i = k_1 v + k_2 v^{1/2} \tag{2}$$

where k_1 and k_2 are adjustable variables derived by plotting $i/v^{1/2}$ *versus* $v^{1/2}$ at various fixed voltages (V). Additionally, $k_1 v$ and $k_2 v^{1/2}$ represent capacitive- and diffusion-controlled currents, respectively.[53] We illustrate the capacitive-controlled current calculated using eq 2 as the filled area relative to the total scanned current at a scan rate of 0.1 mV s^{-1} (Figure 6C, Figure S12). The capacitive contribution of the ZDC at 0.1 mV s^{-1} was 45%, exceeding that of CMK-3 (34%), indicating that the K^+ storage mechanism of the ZDC is predominantly capacitive-controlled. The ZDC also demonstrated a significantly higher capacitive contribution than CMK-3 at all scan rates from 0.1 to 10 mV s^{-1} (Figure 6D). Furthermore, EIS and GITT tests were conducted to further analyze the resistances and K^+ transfer kinetics of the porous carbon anodes (Figure 6E,F). In the Nyquist plots obtained from the EIS analysis, the semicircles represent the charge transfer resistance (R_{CT}) at the electrolyte−electrode interface.[54] ZDC exhibited a significantly smaller R_{CT} than CMK-3. During the potassiation/depotassiation steps, ZDC exhibited lower electrode internal resistance than CMK-3 (Figure 6G), whereas its solid-state diffusion coefficient of K^+ was notably higher than that of CMK-3 (Figure 6H). These results demonstrate that the kinetics of ZDC are superior to those of CMK-3.

Based on the GCD, CV, EIS, and GITT analyses, we demonstrated that ZDC possesses high K^+ storage capacity and enhanced kinetic performance due to the significant contribution of capacitive K^+ storage. To understand this phenomenon, we compared the factors affecting the capacitive K^+ storage in carbon anode materials, including surface area, pore volume, defects, and heteroatom content (Table S4). The influence of interlayer spacing can be neglected because the values are similar for both ZDC and CMK-3. The capacitive K^+ storage capacity is predominantly influenced by the ultramicropore volume rather than the surface area or total pore volume. Ultramicropores (pore width <0.7 nm) can significantly augment the capacitive K^+ storage capacity by facilitating closer proximity of the ion center to the carbon surface.[55,56] As corroborated by CO_2 physisorption results in Figure S13, ZDC exhibits a larger volume of ultramicropores despite possessing a smaller surface area than CMK-3. The formation of ultramicropores in ZDC is due to the Zn ion pairs or clusters in ZnBD acting as molecular templates, generating a substantial amount of (ultra)micropores upon removal by hydrochloric acid washing.[57] Furthermore, the Raman spectra revealed a low (I_D/I_G) ratio and broad G-band line width in ZDC, indicating a relatively higher defect density than in CMK-3.[37] Additionally, the elevated N and O content in ZDC enhances surface-driven K^+ storage, as carbonyl (C═O) groups can store K^+ via the chemical reaction, CO + K^+ + e^- ⇄ C−O−K, and pyridine nitrogen facilitates K^+ adsorption (Table S4).[40,58] Consequently, the prevalence of ultramicropores, defects, and heteroatom-doped sites substantially enhances the capacitive K^+ capacity of ZDC.

CONCLUSIONS

This study successfully demonstrated the large-scale synthesis of high-quality ZnBD crystals under ambient conditions, leveraging the versatility of zinc acetate salts. By harnessing the unique structural properties of acetate salts and their resulting acetate anions as byproducts, we established an optimal environment for ZnBD production. Acetate salts, structurally similar to the SBUs of ZnBD, rapidly reacted with organic ligands at room temperature, initiating the rapid nucleation of ZnBD crystals. During this nucleation process, the dissociated acetate anions acted as crystallization modulators, facilitating the deprotonation of H_2BDC and regulating the crystal growth mode, resulting in anisotropic rod-shaped morphologies. Notably, higher reactant concentrations increased the productivity of ZnBDs without compromising the quality of the MOFs, as confirmed by SEM, XRD, and N_2 sorption analyses. This approach enabled the synthesis of ZnBD crystals on a scale of tens of grams with a STY comparable to those reported for other large-scale MOF syntheses. The synthesized ZnBDs were subsequently converted into highly nanoporous carbons doped with nitrogen and oxygen through a simple thermal treatment, demonstrating their potential as anodes for PIBs. Still, challenges remain for scaling up the synthesis to quantities of tens of kilograms or more. These include developing a continuous synthesis process and optimizing the washing and solvent removal procedures for larger quantities. However, given the energy-efficient synthesis process and the potential of MOF products in energy storage systems, this strategy offers a promising pathway for enhancing the accessibility and application of MOFs in various practical fields such as electrodes for PIBs and capacitive deionization, and adsorbents for various molecules.

ASSOCIATED CONTENT

Supporting Information

The Supporting Information is available free of charge at https://pubs.acs.org/doi/10.1021/acssuschemeng.4c06002.

Kagome crystal structures; additional TEM, SEM images, ^{1}H NMR, XRD, XPS, N_2, CO_2 physisorption,

https://doi.org/10.1021/acssuschemeng.4c06002
ACS Sustainable Chem. Eng. 2024, 12, 14524−14533

CV profiles, and GCD profiles for the ZnBDs and carbons; tables for surface area, pore volume, production yields, space-time yields, and physicochemical properties of ZnBDs and carbons (PDF)

AUTHOR INFORMATION

Corresponding Author

Jongkook Hwang − *Department of Energy Systems Research, Ajou University, Suwon 16499, Korea; Department of Chemical Engineering, Ajou University, Suwon 16499, Korea;* orcid.org/0000-0003-0953-8272; Email: jongkook@ajou.ac.kr

Authors

Giwook Lee − *Department of Energy Systems Research, Ajou University, Suwon 16499, Korea;* orcid.org/0000-0002-5393-2616

Kangseok Kim − *Department of Energy Systems Research, Ajou University, Suwon 16499, Korea*

Eunho Lim − *Department of Chemical & Biochemical Engineering, Dongguk University, Seoul 04620, Korea;* orcid.org/0000-0002-5255-2320

Complete contact information is available at: https://pubs.acs.org/10.1021/acssuschemeng.4c06002

Author Contributions

‡G.L. and K.K. contributed equally. The manuscript was written through contributions of all authors. All authors have given approval to the final version of the manuscript.

Notes

The authors declare no competing financial interest.

ACKNOWLEDGMENTS

This research was supported by the National Research Foundation of Korea (NRF) funded by the Korea Government (Grant 2021R1C1C1009988), Global-Learning & Academic Research Institution for Master's·Ph.D. students, and Postdocs (G-LAMP) Program of the National Research Foundation of Korea (NRF) funded by the Ministry of Education (Grant RS-2023-00285390), and H2KOREA funded by the Ministry of Education (2022Hydrogen fuel cell-002, Innovative Human Resources Development Project for Hydrogen Fuel Cells).

REFERENCES

(1) Li, M.; Li, D.; O'Keeffe, M.; Yaghi, O. M. Topological Analysis of Metal-Organic Frameworks with Polytopic Linkers and/or Multiple Building Units and the Minimal Transitivity Principle. *Chem. Rev.* **2014**, *114* (2), 1343−1370.

(2) ZareKarizi, F.; Joharian, M.; Morsali, A. Pillar-Layered MOFs: Functionality, Interpenetration, Flexibility and Applications. *J. Mater. Chem. A* **2018**, *6* (40), 19288−19329.

(3) Furukawa, H.; Müller, U.; Yaghi, O. M. "Heterogeneity within Order" in Metal-Organic Frameworks. *Angew. Chem., Int. Ed.* **2015**, *54* (11), 3417−3430.

(4) Dybtsev, D. N.; Chun, H.; Kim, K. Rigid and Flexible: A Highly Porous Metal-Organic Framework with Unusual Guest-Dependent Dynamic Behavior. *Angew. Chem., Int. Ed.* **2004**, *43* (38), 5033−5036.

(5) Chun, H.; Moon, J. Discovery, Synthesis, and Characterization of an Isomeric Coordination Polymer with Pillared Kagome Net Topology. *Inorg. Chem.* **2007**, *46* (11), 4371−4373.

(6) Bárcia, P. S.; Zapata, F.; Silva, J. A. C.; Rodrigues, A. E.; Chen, B. Kinetic Separation of Hexane Isomers by Fixed-Bed Adsorption with a Microporous Metal-Organic Framework. *J. Phys. Chem. B* **2007**, *111* (22), 6101−6103.

(7) Schneemann, A.; Vervoorts, P.; Hante, I.; Tu, M.; Wannapaiboon, S.; Sternemann, C.; Paulus, M.; Wieland, D. C. F.; Henke, S.; Fischer, R. A. Different Breathing Mechanisms in Flexible Pillared-Layered Metal-Organic Frameworks: Impact of the Metal Center. *Chem. Mater.* **2018**, *30* (5), 1667−1676.

(8) Hwang, J.; Lee, H.-C.; Antonietti, M.; Schmidt, B. V. K. J. Free Radical and RAFT Polymerization of Vinyl Esters in Metal-Organic-Frameworks. *Polym. Chem.* **2017**, *8* (40), 6204−6208.

(9) Hwang, J.; Heil, T.; Antonietti, M.; Schmidt, B. V. K. J. Morphogenesis of Metal-Organic Mesocrystals Mediated by Double Hydrophilic Block Copolymers. *J. Am. Chem. Soc.* **2018**, *140* (8), 2947−2956.

(10) Hwang, J.; Yan, R.; Oschatz, M.; Schmidt, B. V. K. J. Solvent Mediated Morphology Control of Zinc MOFs as Carbon Templates for Application in Supercapacitors. *J. Mater. Chem. A* **2018**, *6* (46), 23521−23530.

(11) Chaemchuen, S.; Zhou, K.; Yusubov, M. S.; Postnikov, P. S.; Klomkliang, N.; Verpoort, F. Solid-State Transformation in Porous Metal-Organic Frameworks Based on Polymorphic-Pillared Net Structure: Generation of Tubular Shaped MOFs. *Microporous Mesoporous Mater.* **2019**, *278*, 99−104.

(12) Kim, T.; Kim, K.; Lee, G.; Seo, M.; Hwang, J. Guidelines for the Design of Solid CO2 Adsorbents for Mobile Carbon Capture in Heavy-Duty Vehicles: A Review. *Korean J. Chem. Eng.* **2024**, *41* (1), 25−42.

(13) Kaneti, Y. V.; Tang, J.; Salunkhe, R. R.; Jiang, X.; Yu, A.; Wu, K. C.-W.; Yamauchi, Y. Nanoarchitectured Design of Porous Materials and Nanocomposites from Metal-Organic Frameworks. *Adv. Mater.* **2017**, *29* (12), 1604898.

(14) Hwang, J.; Ejsmont, A.; Freund, R.; Goscianska, J.; Schmidt, B.; Wuttke, S. Controlling the Morphology of Metal-Organic Frameworks and Porous Carbon Materials: Metal Oxides as Primary Architecture-Directing Agents. *Chem. Soc. Rev.* **2020**, *49* (11), 3348−3422.

(15) Wang, C.; Kim, J.; Tang, J.; Na, J.; Kang, Y.-M.; Kim, M.; Lim, H.; Bando, Y.; Li, J.; Yamauchi, Y. Large-Scale Synthesis of MOF-Derived Superporous Carbon Aerogels with Extraordinary Adsorption Capacity for Organic Solvents. *Angew. Chem., Int. Ed.* **2020**, *59* (5), 2066−2070.

(16) Jagadeesh, R. V.; Murugesan, K.; Alshammari, A. S.; Neumann, H.; Pohl, M.-M.; Radnik, J.; Beller, M. MOF-Derived Cobalt Nanoparticles Catalyze a General Synthesis of Amines. *Science* **2017**, *358* (6361), 326−332.

(17) Rubio-Martinez, M.; Avci-Camur, C.; Thornton, A. W.; Imaz, I.; Maspoch, D.; Hill, M. R. New Synthetic Routes towards MOF Production at Scale. *Chem. Soc. Rev.* **2017**, *46* (11), 3453−3480.

(18) Ren, J.; Dyosiba, X.; Musyoka, N. M.; Langmi, H. W.; Mathe, M.; Liao, S. Review on the Current Practices and Efforts towards Pilot-Scale Production of Metal-Organic Frameworks (MOFs). *Coord. Chem. Rev.* **2017**, *352*, 187−219.

(19) Rasmussen, E. G.; Kramlich, J.; Novosselov, I. V. Scalable Continuous Flow Metal-Organic Framework (MOF) Synthesis Using Supercritical CO_2. *ACS Sustain. Chem. Eng.* **2020**, *8* (26), 9680−9689.

(20) Chakraborty, D.; Yurdusen, A.; Mouchaham, G.; Nouar, F.; Serre, C. Large-Scale Production of Metal-Organic Frameworks. *Adv. Funct. Mater.* **2023**, 2309089.

(21) Zhou, K.; Chaemchuen, S.; Wu, Z.; Verpoort, F. Rapid Room Temperature Synthesis Forming Pillared Metal-Organic Frameworks with Kagomé Net Topology. *Microporous Mesoporous Mater.* **2017**, *239*, 28−33.

(22) Tranchemontagne, D. J.; Hunt, J. R.; Yaghi, O. M. Room Temperature Synthesis of Metal-Organic Frameworks: MOF-5, MOF-74, MOF-177, MOF-199, and IRMOF-0. *Tetrahedron* **2008**, *64* (36), 8553−8557.

(23) Hungerford, J.; Walton, K. S. Room-Temperature Synthesis of Metal-Organic Framework Isomers in the Tetragonal and Kagome Crystal Structure. *Inorg. Chem.* **2019**, *58* (12), 7690−7697.

(24) Serre, C.; Millange, F.; Surblé, S.; Férey, G. A Route to the Synthesis of Trivalent Transition-Metal Porous Carboxylates with

Trimeric Secondary Building Units. *Angew. Chem., Int. Ed.* **2004**, *43* (46), 6285−6289.
(25) Guillerm, V.; Gross, S.; Serre, C.; Devic, T.; Bauer, M.; Férey, G. A Zirconium Methacrylate Oxocluster as Precursor for the Low-Temperature Synthesis of Porous Zirconium(iv) Dicarboxylates. *Chem. Commun.* **2010**, *46* (5), 767−769.
(26) Cravillon, J.; Schröder, C. A.; Nayuk, R.; Gummel, J.; Huber, K.; Wiebcke, M. Fast Nucleation and Growth of ZIF-8 Nanocrystals Monitored by Time-Resolved In Situ Small-Angle and Wide-Angle X-Ray Scattering. *Angew. Chem., Int. Ed.* **2011**, *50* (35), 8067−8071.
(27) Wagia, R.; Strashnov, I.; Anderson, M. W.; Attfield, M. P. Determination of the Preassembled Nucleating Units That Are Critical for the Crystal Growth of the Metal-Organic Framework CdIF-4. *Angew. Chem., Int. Ed.* **2016**, *55* (31), 9075−9079.
(28) Lee, G.; Hwang, J. Direct Synthesis of Mixed-Metal Paddle-Wheel Metal-Organic Frameworks with Controlled Metal Ratios under Ambient Conditions. *Inorg. Chem.* **2023**, *62* (48), 19457−19465.
(29) Shekhah, O.; Wang, H.; Paradinas, M.; Ocal, C.; Schüpbach, B.; Terfort, A.; Zacher, D.; Fischer, R. A.; Wöll, C. Controlling Interpenetration in Metal-Organic Frameworks by Liquid-Phase Epitaxy. *Nat. Mater.* **2009**, *8* (6), 481−484.
(30) Shekhah, O.; Wang, H.; Zacher, D.; Fischer, R. A.; Woll, C. Growth Mechanism of Metal-Organic Frameworks: Insights into the Nucleation by Employing a Step-by-Step Route. *Angew. Chem., Int. Ed.* **2009**, *48* (27), 5038−41.
(31) Jun, S.; Joo, S. H.; Ryoo, R.; Kruk, M.; Jaroniec, M.; Liu, Z.; Ohsuna, T.; Terasaki, O. Synthesis of New, Nanoporous Carbon with Hexagonally Ordered Mesostructure. *J. Am. Chem. Soc.* **2000**, *122* (43), 10712−10713.
(32) Yue, Y.; Qiao, Z. A.; Fulvio, P. F.; Binder, A. J.; Tian, C.; Chen, J.; Nelson, K. M.; Zhu, X.; Dai, S. Template-Free Synthesis of Hierarchical Porous Metal-Organic Frameworks. *J. Am. Chem. Soc.* **2013**, *135* (26), 9572−5.
(33) Huo, J.; Brightwell, M.; El Hankari, S.; Garai, A.; Bradshaw, D. A Versatile, Industrially Relevant, Aqueous Room Temperature Synthesis of HKUST-1 with High Space-Time Yield. *J. Mater. Chem. A* **2013**, *1* (48), 15220−15223.
(34) Jiang, D.; Huang, C.; Zhu, J.; Wang, P.; Liu, Z.; Fang, D. Classification and Role of Modulators on Crystal Engineering of Metal Organic Frameworks (MOFs). *Coord. Chem. Rev.* **2021**, *444*, 214064.
(35) Ning, J.; Kershaw, S. V.; Rogach, A. L. Synthesis of Anisotropic ZnSe Nanorods with Zinc Blende Crystal Structure. *Angew. Chem., Int. Ed.* **2020**, *59* (13), 5385−5391.
(36) Sivakumar, A.; Jude Dhas, S. S.; Pazhanivel, T.; Almansour, A. I.; Kumar, R. S.; Arumugam, N.; Raj, C. J.; Dhas, S. A. M. B. Phase Transformation of Amorphous to Crystalline of Multiwall Carbon Nanotubes by Shock Waves. *Cryst. Growth Des.* **2021**, *21* (3), 1617−1624.
(37) Ferrari, A. C.; Robertson, J. Interpretation of Raman Spectra of Disordered and Amorphous Carbon. *Phys. Rev. B* **2000**, *61* (20), 14095−14107.
(38) Kim, S.; Ju, M.; Lee, J.; Hwang, J.; Lee, J. Polymer Interfacial Self-Assembly Guided Two-Dimensional Engineering of Hierarchically Porous Carbon Nanosheets. *J. Am. Chem. Soc.* **2020**, *142* (20), 9250−9257.
(39) Chen, J.; Yang, B.; Li, H.; Ma, P.; Lang, J.; Yan, X. Candle Soot: Onion-Like Carbon, an Advanced Anode Material for a Potassium-Ion Hybrid Capacitor. *J. Mater. Chem. A* **2019**, *7* (15), 9247−9252.
(40) Chong, S.; Yuan, L.; Li, T.; Shu, C.; Qiao, S.; Dong, S.; Liu, Z.; Yang, J.; Liu, H. K.; Dou, S. X.; Huang, W. Nitrogen and Oxygen Co-Doped Porous Hard Carbon Nanospheres with Core-Shell Architecture as Anode Materials for Superior Potassium-Ion Storage. *Small* **2022**, *18* (8), 2104296.
(41) Hwang, J.; Walczak, R.; Oschatz, M.; Tarakina, N. V.; Schmidt, B. V. K. J. Micro-Blooming: Hierarchically Porous Nitrogen-Doped Carbon Flowers Derived from Metal-Organic Mesocrystals. *Small* **2019**, *15* (37), 1901986.
(42) Zhang, W.; Liu, Y.; Guo, Z. Approaching High-Performance Potassium-Ion Batteries via Advanced Design Strategies and Engineering. *Sci. Adv.* **2019**, *5* (5), No. eaav7412.
(43) Kim, K.; Park, J.; Lee, J.; Lim, E.; Hwang, J. Direct Microstructure Tailoring of Hard Carbon Electrodes for Fabrication of Dual-Carbon Potassium-Ion Hybrid Supercapacitors. *Energy Fuels* **2024**, *38* (9), 8285−8295.
(44) Liang, Z.; Gao, S.; Liu, Y.; Qiu, T.; Shao, Y.; Qin, R.; Cheng, J.; Tang, Y.; Wu, Y.; Shi, J.; Pan, F.; Zou, R. Dual Heteroatom-Doping-Induced Potassium Storage Enhancement in a Hierarchical Carbon Nanorod-Assembled Superstructure. *ACS Sustain. Chem. Eng.* **2022**, *10* (47), 15350−15356.
(45) Xiong, P.; Zhao, X.; Xu, Y. Nitrogen-Doped Carbon Nanotubes Derived from Metal-Organic Frameworks for Potassium-Ion Battery Anodes. *ChemSusChem* **2018**, *11* (1), 202−208.
(46) Yang, J.; Ju, Z.; Jiang, Y.; Xing, Z.; Xi, B.; Feng, J.; Xiong, S. Enhanced Capacity and Rate Capability of Nitrogen/Oxygen Dual-Doped Hard Carbon in Capacitive Potassium-Ion Storage. *Adv. Mater.* **2018**, *30* (4), 1700104.
(47) Li, Y.; Yang, C.; Zheng, F.; Ou, X.; Pan, Q.; Liu, Y.; Wang, G. High Pyridine N-doped Porous Carbon Derived from Metal-Organic Frameworks for Boosting Potassium-Ion Storage. *J. Mater. Chem. A* **2018**, *6* (37), 17959−17966.
(48) Liang, Z.; Wu, Y.; Cheng, J.; Tang, Y.; Shi, J.; Qiu, T.; Li, W.; Gao, S.; Zhong, R.; Zou, R. A Metal-Organic Framework Nanorod-Assembled Superstructure and Its Derivative: Unraveling the Fast Potassium Storage Mechanism in Nitrogen-Modified Micropores. *Small* **2021**, *17* (19), 2100135.
(49) Li, J.; Li, Y.; Ma, X.; Zhang, K.; Hu, J.; Yang, C.; Liu, M. A Honeycomb-Like Nitrogen-Doped Carbon as High-Performance Anode for Potassium-Ion Batteries. *Chem. Eng. J.* **2020**, *384*, 123328.
(50) Zhou, X.; Chen, L.; Zhang, W.; Wang, J.; Liu, Z.; Zeng, S.; Xu, R.; Wu, Y.; Ye, S.; Feng, Y. Three-Dimensional Ordered Macroporous Metal-Organic Framework Single Crystal-Derived Nitrogen-Doped Hierarchical Porous Carbon for High-Performance Potassium-Ion Batteries. *Nano Lett.* **2019**, *19* (8), 4965−4973.
(51) Tong, H.; Wang, C.; Lu, J.; Chen, S.; Yang, K.; Huang, M.; Yuan, Q.; Chen, Q. Energetic Metal-Organic Frameworks Derived Highly Nitrogen-Doped Porous Carbon for Superior Potassium Storage. *Small* **2020**, *16* (43), 2002771.
(52) Augustyn, V.; Come, J.; Lowe, M. A.; Kim, J. W.; Taberna, P.-L.; Tolbert, S. H.; Abruña, H. D.; Simon, P.; Dunn, B. High-Rate Electrochemical Energy Storage through Li^+ Intercalation Pseudocapacitance. *Nat. Mater.* **2013**, *12* (6), 518−522.
(53) Yan, X.; Wang, F.; Su, X.; Ren, J.; Qi, M.; Bao, P.; Chen, W.; Peng, C.; Chen, L. A Redox-Active Covalent Organic Framework with Highly Accessible Aniline-Fused Quinonoid Units Affords Efficient Proton Charge Storage. *Adv. Mater.* **2023**, *35* (44), 2305037.
(54) Park, J.; Kim, K.; Lim, E.; Hwang, J. Tuning Internal Accessibility via Nanochannel Orientation of Mesoporous Carbon Spheres for High-Rate Potassium-Ion Storage in Hybrid Supercapacitors. *Adv. Funct. Mater.* **2024**, 2410010.
(55) Chmiola, J.; Yushin, G.; Gogotsi, Y.; Portet, C.; Simon, P.; Taberna, P.-L. Anomalous Increase in Carbon Capacitance at Pore Sizes Less than 1 Nanometer. *Science* **2006**, *313* (5794), 1760−1763.
(56) Lee, J.; Park, J.; Lim, E.; Hwang, J. Unveiling the Impact of Ultramicropores in Carbonaceous Electrode Materials to Boost Surface-Driven Capacitive Potassium Ion Storage in Hybrid Supercapacitors. *Appl. Surf. Sci.* **2024**, *645*, 158875.
(57) Youk, S.; Hofmann, J. P.; Badamdorj, B.; Völkel, A.; Antonietti, M.; Oschatz, M. Controlling Pore Size and Pore Functionality in sp^2-Conjugated Microporous Materials by Precursor Chemistry and Salt Templating. *J. Mater. Chem. A* **2020**, *8* (41), 21680−21689.
(58) Liu, Z.; Wu, S.; Song, Y.; Yang, T.; Ma, Z.; Tian, X.; Liu, Z. Non-Negligible Influence of Oxygen in Hard Carbon as an Anode Material for Potassium-Ion Batteries. *ACS Appl. Mater. Interfaces* **2022**, *14* (42), 47674−47684.

https://doi.org/10.1021/acssuschemeng.4c06002
ACS Sustainable Chem. Eng. 2024, 12, 14524−14533